High resolution method for direct numerical simulation of the instability and transition in a baroclinic cavity

Anthony Randriamampianina, Emilia Crespo del Arco

A High-Resolution Method for Direct Numerical Simulation of Instabilities and Transitions in a Baroclinic Cavity

Anthony Randriamampianina[1] and Emilia Crespo del Arco[2]

16.1. INTRODUCTION

Baroclinic instability is recognized to be one of the dominant energetic processes in the large-scale atmospheres of terrestrial planets, such as Earth and Mars, e.g., *Pierrehumbert and Swanson* [1995], and in the oceans. Its fully developed form as sloping convection is strongly nonlinear and has a major role in the transport of heat and momentum in the atmospheric and oceanic motions. Its time-dependent behavior also exerts a dominant influence on the intrinsic predictability of the atmosphere and the degree of chaotic variability in its large-scale meteorology [e.g, *Pierrehumbert and Swanson*, 1995; *Read et al.*, 1998; *Read*, 2001]. On the other hand, the close analogy between the dynamics of the ocean and atmosphere has been reported by *Orlanski and Cox* [1973]: "Similar phenomena take place from the high frequency range characterized by internal gravity waves to the low range of frequencies dominated by quasi-geostrophic motion. Detailed temperature measurements indicate that the ocean has relatively large-scale density discontinuities that are very much like atmospheric fronts. The oceanic fronts have a characteristic slope which is determined by the density difference, rotation and vertical shear of the currents parallel to the front. Since atmospheric fronts are known to be baroclinically unstable, it appears to be appropriate to suspect the same mechanism may be present in the ocean."

Since the pioneering works of *Hide* [1958] in the 1950s, the differentially heated, rotating cylindrical annulus has been an archetypal means of studying the properties of fully developed baroclinic instability in the laboratory. The system is well known to exhibit a rich variety of different flow regimes, depending upon the imposed conditions (primarily the temperature contrast ΔT and rotation rate Ω), ranging from steady, axisymmetric circulations through highly symmetric, regular wave flows to fully developed geostrophic turbulence [*Hide*, 1958; *Fowlis and Hide*, 1965].

With the exponential increase in computing power these last decades, direct numerical simulation has become an indispensable tool for investigating the complex spatiotemporal behaviors of baroclinic instability in the laboratory, complementarily with experiments. Even though it does not yet allow for a complete study of the fully developed turbulent regimes, it provides new insight into the mechanisms responsible for these disordered flows. Moreover, direct numerical simulation, free of uncertainties related to turbulence modelings and of imperfections of experimental setups, can supply more extensive data than measurements and thus facilitate the detailed analysis of the wave dynamics. In particular, it is useful to explore the different nonlinear flow regimes in the parameter space in order to accurately delineate a bifurcation diagram. Moreover, direct numerical simulation provides relevant information about the small-scale fluctuations that progressively destroy the regularity of the flow during the transition toward geostrophic turbulence. Thereby it can efficiently serve as a guide to experiments and also supplement measurements.

16.2. NUMERICAL MODEL

16.2.1. Background

The first numerical investigations devoted to baroclinic waves in the differentially heated rotating cylindrical annulus were reported by *Williams* [1969] based on

1Laboratoire Mécanique, Modélisation & Procédés Propres, UMR 7340 CNRS, Aix Marseille Université, Marseille, France.

2Departamento de Física Fundamental, Universidad Nacional de Educación a Distancia (UNED), Madrid, Spain.

a second-order finite difference approximation in space and in time. The approach was implemented on staggered grids over a regular mesh for the pressure-temperature and the velocity components. An explicit second-order leap-frog scheme was employed to discretize both the space and time derivatives. However the integration domain was restricted to a sector, only admitting the dominant wave and its harmonics. The cavity was filled with water, assumed to satisfy the Boussinesq approximation, with the density variation applied to the gravitational acceleration [*Williams*, 1971].

Then *James et al.* [1981] carried out a combined laboratory and numerical study of the steady baroclinic waves. Similar to the model proposed by *Williams* [1969], staggered grids were used with a second-order finite difference formula, but without any arbitrary truncation of the full spectrum of the waves. A hyperbolic tangent transformation was introduced to stretch the mesh toward the boundaries in the radial and axial directions while keeping uniform distribution in the azimuthal direction with Fourier series. To avoid severe constraint on the time step stability condition associated with these small grid sizes within the boundary layers, a Dufort-Frankel scheme was used for the diffusion terms, taking into account eventual variations of the viscosity, unlike the formulation of *Williams* [1969]. Using a water-glycerol mixture as working fluid, properties were assumed variable, with quadratic and linear dependencies with the temperature respectively for the density and for the kinematic viscosity and the thermal diffusivity. However, the authors did not achieve direct comparison of results between experiment and numerical simulation under the same external conditions, partially inferred to the restricted coarse resolutions used, due to the existing computer capacity constraints.

Hignett et al. [1985] continued these studies and obtained the same wave flow structure under identical conditions for the laboratory experiment and numerical simulation by using a different combination of water and glycerol than *James et al.* [1981]. They introduced density variations in centrifugal acceleration, contrary to *James et al.* [1981]. They put forward the intransitivity of the flow for steady wave state, corresponding to the coexistence of different stable wave structures under the same external conditions. They also mentioned the occurrence of hysteresis cycles during the transition from axisymmetric to nonaxisymmetric solutions, as already observed by *Hide* [1958] with an open upper free-surface configuration.

A sophisticated version, *MORALS (Met Office/Oxford Rotating Annulus Laboratory Simulation)*, derived from the numerical tool proposed by *James et al.* [1981], was implemented at the University of Oxford, UK (AOPP), for the investigations of a wide spectrum of applications devoted to geophysical fluid dynamics.

The choice of high-resolution spectral technique in the present study stems from its ability to accurately predict the thresholds of the different bifurcations occurring during time-dependent flow regimes, resulting from its global character, in contrast with local finite difference discretization [*Gottlieb and Orszag*, 1977; *Canuto et al.*, 1987]. In particular, the accuracy of spectral techniques was discussed in detail by *Pulicani et al.* [1990] (see also *Randriamampianina et al.* [1990]) during the simulation of oscillatory convection at low Prandtl number. Moreover, the approach is well suited for the simulation of rotating flows in enclosures, where the boundary layer is three dimensional from its inception.

16.2.2. Governing Equations

The physical model, the so-called baroclinic cavity, consists of an annular domain of inner radius a, outer radius b, and height d rotating around its vertical axis of symmetry. The cavity is filled with a liquid defined by a Prandtl number Pr and is submitted to a temperature difference $\Delta T = T_b - T_a$ between the inner, cold, and outer, hot, cylinders closed by horizontal insulating rigid endplates. One specific configuration involving an open upper free surface is also considered.

In the meridional plane, the dimensional space variables $(r^*, z^*) \in [a, b] \times [0, d]$ have been normalized into the square $[-1, 1] \times [-1, 1]$, a prerequisite for the use of Chebyshev polynomials (where the asterisk denotes dimensional variables):

$$r = \frac{2r^*}{b-a} - \frac{b+a}{b-a}, \qquad z = \frac{2z^*}{d} - 1.$$

The fluid is assumed to satisfy the Boussinesq approximation [*Zeytounian*, 2003] with constant properties except for the density when applied to the Coriolis, centrifugal, and gravitational accelerations, where $\rho^* = \rho_0[1-\alpha(T^*-T_0)]$, where α is the coefficient of thermal expansion and T_0 is a reference temperature $T_0 = (T_b + T_a)/2$. However, it was found that the contribution of density variation with the Coriolis term $\rho_0 \alpha T^* \Omega \mathbf{e}_z \times \mathbf{V}^*$ was negligible compared to the centrifugal and gravitational ones. Moreover, for the imposed external conditions, the variations with temperature of viscosity and thermal diffusivity remain small, keeping the value of Prandtl number almost constant (at least below the margins of error from measurements). The reference scales are the velocity $U^* = g\alpha\, \Delta T/2\Omega$ and the time $t^* = (2\Omega)^{-1}$, and the nondimensional normalized temperature is $2(T^* - T_0)/\Delta T$ [*Randriamampianina et al.*, 2006].

Depending on the type of solution sought, axisymmetric or nonaxisymmetric, two different approaches are considered independently for the governing equations of the flow dynamics. In the first case, a vorticity stream function

Table 16.1. Summary of the dimensions of the system, the fluid properties, and the governing parameters for the liquid-filled cavity: Pr = 16.

Inner radius	a	4.5 cm
Outer radius	b	15. cm
Height	d	26. cm
Gap width	$L = b - a$	10.5 cm
Mean temperature	T_0	293 K
Temperature difference	$\Delta T = T_b - T_a$	2 K
Rotation rate	Ω	0.25–1.25 rad/s
Volume expansion coefficient	α	3.171×10^{-4} K^{-1}
Kinematic viscosity	ν	2.0397×10^{-2} cm^2/s
Thermal diffusivity	κ	1.2731×10^{-3} cm^2/s
Aspect ratio	$A = d/L$	2.47619
Curvature parameter	$R_C = (b + a)/L$	1.857
Prandtl number	$\mathrm{Pr} = \nu/\kappa$	16.0215
Rayleigh number	$\mathrm{Ra} = g\alpha\,\Delta T\,L^3/(\nu\kappa)$	2.7735×10^7
Froude number	$\mathrm{Fr} = \Omega^2 L/g$	6.69×10^{-4}–1.67×10^{-2}
Taylor number	$\mathrm{Ta} = 4\Omega^2 L^5/(\nu^2 d)$	$2.95 \times 10^6 - 7.37 \times 10^7$
Thermal Rossby number	$\Theta = g\,d\alpha\,\Delta T/(\Omega^2 L^2)$	2.3475–0.0939

with azimuthal velocity formulation is introduced. Not only does it reduce the number of equations to solve, in comparison with the primitive variable velocity-pressure formulation, but it also ensures a divergence-free velocity field irrespective of the mesh used. An influence matrix technique is implemented to treat the lack of boundary conditions for the vorticity coupled with the stream function [*Chaouche et al.*, 1990; *Randriamampianina et al.*, 2001, 2004]. For the three-dimensional solution, the primitive variables are directly solved. We present hereafter the details of the governing equations and the numerical method for the latter.

In a frame of reference rotating with the cavity, the resulting dimensionless system is written as [*Randriamampianina et al.*, 2006]

$$\frac{\partial \mathbf{V}}{\partial t} + \frac{2\,\mathrm{Ra}}{A^2\,\mathrm{Pr}\,\mathrm{Ta}} N(\mathbf{V}) + \mathbf{e}_z \times \mathbf{V} = -\nabla \Pi + \frac{4}{A^{3/2}\,\mathrm{Ta}^{1/2}} \nabla^2 \mathbf{V} + \mathbf{F}, \tag{16.1}$$

$$\nabla \cdot \mathbf{V} = 0, \tag{16.2}$$

$$\frac{\partial T}{\partial t} + \frac{2\,\mathrm{Ra}}{A^2\,\mathrm{Pr}\,\mathrm{Ta}} \nabla.(\mathbf{V}T) = \frac{4}{A^{3/2}\,\mathrm{Pr}\,\mathrm{Ta}^{1/2}} \nabla^2 T, \tag{16.3}$$

with

$$\Pi = \frac{p + \rho_0 g z - \frac{1}{2}\rho_0 \Omega^2 r^2}{\rho_0 g \alpha\,\Delta T\,d/2},$$

$$\mathbf{F} = \frac{1}{2} T \mathbf{e}_z - \frac{\mathrm{Fr}}{4A}\,(r + R_c)\,T \mathbf{e}_r,$$

where $\mathbf{e}_r$ and $\mathbf{e}_z$ are the unit vectors in the radial and axial directions, respectively, and $N(\mathbf{V})$ represents the nonlinear advection terms. The parameters governing the flow and the heat transfer are the aspect ratio A, the curvature parameter R_c, the Prandtl number Pr, the Rayleigh number Ra, the Froude number Fr, and the Taylor number Ta (see the definitions in Table 16.1). For a given fluid within a fixed geometry, the Taylor number is one of the two main control parameters traditionally used to analyze this system, following, e.g., *Fowlis and Hide* [1965] and *Hide and Mason* [1975]. The second parameter is the thermal Rossby number,

$$\Theta = \frac{g\,d\alpha\,\Delta T}{\Omega^2 (b-a)^2} \equiv \frac{4\,\mathrm{Ra}}{\mathrm{Pr}\,\mathrm{Ta}},$$

introduced by *Hide* [1958] as a stability parameter, which gives a measure of the buoyancy strength over the Coriolis term and appears explicitly as coefficient o f the advection terms in equations (16.1) and (16.3).

The "skew-symmetric" form proposed by *Zang* [1990] was chosen for the nonlinear advection term $N(\mathbf{V}) = [\mathbf{V}.\nabla\mathbf{V} + \nabla.(\mathbf{V}\mathbf{V})]/2$ in the momentum equation (16.1) to ensure the conservation of kinetic energy, a necessary condition for a simulation to be numerically stable in time.

16.2.3. Boundary Conditions

The boundary conditions are no-slip velocity conditions at all rigid surfaces,

$$\mathbf{V} = \mathbf{0} \quad \text{at } r = \pm 1 \quad \text{and at } z = \pm 1,$$

thermal insulation at horizontal rigid surfaces,

$$\frac{\partial T}{\partial z} = 0 \quad \text{at } z = \pm 1,$$

and constant-temperature conditions at the vertical sidewalls,

$$T = \pm 1 \quad \text{at } r = \pm 1.$$

In the case of an open upper wall, planar free-surface conditions are imposed, assuming the absence of vertical deformation along this boundary, in agreement with experimental observations for the control parameter values under consideration [*Harlander et al.*, 2011]:

$$\frac{\partial T}{\partial z} = \frac{\partial V_r}{\partial z} = \frac{\partial V_\phi}{\partial z} = V_z = 0 \quad \text{at } z = 1.$$

16.2.4. Solution Method

A pseudospectral collocation Chebyshev method is implemented in the meridional plane (r, z), in association with Galerkin-Fourier approximation in azimuth ϕ for the three-dimensional flow regimes to solve the primitive variable formulation described above. Each dependent variable is expanded in the approximation space $\mathcal{P}_{NM}$, composed of Chebyshev polynomials of degrees less than or equal to N and M in the r and z directions, respectively, while Fourier series are introduced in the azimuthal direction with K modes.

For each dependent variable f ($f \equiv V_r, V_\phi, V_z, T, p$), it reads

$$f_{NMK}(r, \phi, z, t) = \sum_{n=0}^{N} \sum_{m=0}^{M} \sum_{k=-K/2}^{K/2-1} \hat{f}_{nmk}(t) T_n(r) T_m(z) \exp(ik\phi),$$

where T_n and T_m are Chebyshev polynomials of degrees n and m.

This approximation is applied at collocation points, where the differential equations are assumed to be satisfied exactly [*Gottlieb and Orszag*, 1977; *Canuto et al.*, 1987]. We have chosen the Chebyshev-Gauss-Lobatto distribution defined by a high concentration of points toward the boundaries, well suited to handle the thin dynamical and thermal boundary layers expected to develop at high values of the Taylor Ta and Rayleigh Ra numbers, which scale as $\mathrm{Ta}^{-1/4}$ (Ekman layer, along horizontal walls) or $\mathrm{Ta}^{-1/6}$ (Stewartson layer, along vertical cylinders) and $\mathrm{Ra}^{-1/4}$, respectively:

$$r_i = \cos\left(\frac{i\pi}{N}\right) \quad \text{for } i \in [0, N],$$

$$z_j = \cos\left(\frac{j\pi}{M}\right) \quad \text{for } j \in [0, M],$$

and a uniform mesh in the azimuthal direction according to the Fourier series:

$$\phi_k = \frac{2k\pi}{K} \quad \text{for } k \in [0, K].$$

The time integration used is second-order accurate and is based on a combination of Adams-Bashforth (AB) and backward differentiation formula (BDF) schemes, chosen for its good stability properties [*Vanel et al.*, 1986]. The resulting AB/BDF scheme is semi-implicit, and for the transport equation of the velocity components in equation (16.1),

$$\frac{3f^{l+1} - 4f^l + f^{l-1}}{2\,\delta t} + 2\mathcal{N}(f^l) - \mathcal{N}(f^{l-1}) = -\nabla \Pi^{l+1} + \frac{4}{A^{3/2} Ta^{1/2}} \nabla^2 f^{l+1} + F_i^{l+1} \tag{16.4}$$

where $\mathcal{N}(f)$ is a "global term" including the advection terms $N(\mathbf{V})$ and the Coriolis term, F_i corresponds to the component of the forcing term $\mathbf{F}$, δt is the time step, and the superscript l refers to time level. The cross terms in the diffusion part in the (r, ϕ) plane resulting from the use of cylindrical coordinates in equation (16.1) are treated within $\mathcal{N}(f)$. The latter is discretized in time using a second-order explicit AB scheme in order to maintain an overall second-order time accuracy with the BDF scheme applied to the diffusion term, as shown in equation (16.4). An equivalent discretization applies for the transport equation (16.3) of the temperature. For the initial step, we have taken $f^{-1} = f^0$. At each time step, the problem then reduces to the solution of Helmholtz and Poisson equations. We recall that the same time scheme is also implemented for the integration of the axisymmetric system, even though steady state solutions are sought.

An efficient projection scheme is introduced to solve the coupling between the velocity and the pressure in equation (16.1). This algorithm ensures a divergence-free velocity field at each time step, maintains the order of accuracy of the time scheme for each dependent variable and does not require the use of staggered grids [*Hugues and Randriamampianina*, 1998; *Raspo et al.*, 2002]. At each time step, a preliminary Poisson equation for the pressure, directly derived from the Navier-Stokes equations, is first solved before integrating the governing system described above. It allows for a variation in time of the normal pressure gradient at boundaries [*Hugues and Randriamampianina*, 1998], which plays an important role for time-dependent flows, in particular in the presence of an open free surface. A complete diagonalization of operators yields simple matrix products for the solution of successive Helmholtz and Poisson equations at each time step [*Haldenwang et al.*, 1984]. The computations of eigenvalues, eigenvectors, and inversion of corresponding

matrices from these Helmholtz and Poisson operators are performed once during a preprocessing step.

16.2.5. Computational Details

For the transition from the upper symmetric regime to the regular waves, the initial conditions corresponded to the steady axisymmetric solution at each azimuthal node to which a random perturbation was added to the temperature field in azimuth. Subsequently, the strategy consisted of progressively increasing the rotation rate without adding any further perturbations for the computation of the following successive three-dimensional solutions.

The length of time for each specific computed solution strongly depends on the fluid considered, e.g., on the Prandtl number, due to the very different temporal behaviors involved. Some values of the wave drift were reported for air by *Randriamampianina et al.* [2006]. Theoretically, only one drift period of the large-scale baroclinic waves is necessary to have a complete analysis of the flow. But close to a bifurcation, corresponding to significant changes on the flow structure and temporal behavior, several drift periods have been computed until the final state is reached. This was the case during the computations of the different bifurcations occurring at the transition between wave numbers $m = 2$ and $m = 3$ for air, in particular during the bifurcation between the quasi-periodic regimes QP2 and QP3 characterized by two and three incommensurate frequencies, respectively. On the other hand, the presence of small-scale inertia gravity waves in the cases of liquids required much longer drift periods of the baroclinic waves and higher resolutions to ensure grid independency of the solution than for air, therefore increasing the length of integration time to be simulated. The different meshes with the corresponding time step used are reported hereafter for each specific case treated.

For Pr = 16 with $\Delta T = 2$ K at $\Omega = 0.5125$ rad/s, about 7.62×10^{-5} CPU seconds per time step and per mode on the supercomputer *NEC−SX*5 (IDRIS, Orsay, France) were necessary to compute the different scales occurring simultaneously within the cavity once the transient was removed (see hereafter the corresponding time step and mesh used). The transient is assumed to be finished when a clear temporal behavior can be identified from the time evolution of one dependent variable taken at a fixed monitoring point and when its random behavior disappears. The transient is also associated with the flow structure observed.

16.2.6. Validation

The numerical tools have been completely developed by the team [*Chaouche et al.*, 1990; *Hugues and Randriamampianina*, 1998; *Raspo et al.*, 2002]. The three-dimensional solutions were previously validated by *Randriamampianina et al.* [1997] for a liquid-filled cavity (Pr = 13.07) with respect to the detailed results reported by *Hignett et al.* [1985] from a combined laboratory and numerical study. Comparisons have been carried out between our computations and their measurements for a regular steady three-wave flow (characterized by a dominant azimuthal wave number $m = 3$). Very close agreement has been obtained for the qualitative structure of the flow pattern and for the quantitative comparison of the radial variation of the azimuthal velocity at different heights. Particular attention has been paid to the grid effect on the solution, which has served as a basis for subsequent studies.

16.3. RESULTS

Hide [1958] and *Fowlis and Hide* [1965], from their pioneering experimental investigations of baroclinic instability using liquids as working fluids, have delineated three main classes of flow regimes: axisymmetric regimes, regular waves, and irregular waves or geostrophic turbulence (see also *Hide and Mason* [1975]). The regular wave regimes are composed of the steady waves, denoted *S*, and the vacillation regimes subdivided into amplitude vacillation, AV or MAV (modulated amplitude vacillation), and structural vacillation, SV. The steady waves are determined by a dominant azimuthal wave number *m* in space and characterized by periodic oscillations in time induced by the uniform angular drift of the waves with constant amplitude. The amplitude vacillation regimes are defined by periodic (AV), quasi-periodic, or chaotic (MAV) temporal behavior of the amplitude of the dominant wave number (for a detailed analysis of the amplitude vacillation phenomenon, see Chapter 3 in this book). The SV regime, an intermediate step before the transition toward geostrophic turbulence, is characterized by a spatiotemporal chaos but still with a well-defined dominant wave number, as shown by the experimental evidence of *Früh and Read* [1997] (see also *Read et al.* [2008]).

Three specific fluids have been considered in the present study, air, a water-glycerol mixture, and water, in order to get insight into the important role played by the Prandtl number on the spatiotemporal characteristics of the baroclinic instability. Indeed, the Prandtl number Pr is a parameter of particular interest, also in the context of other convection problems. *Fein and Pfeffer* [1976], who carried out a careful survey of the main flow regimes in a thermally driven annulus using mercury, water, or silicon oils, found significant differences in the onset of baroclinic instability in the region of the so-called lower symmetric transition at low Taylor number, where viscous diffusion and thermal diffusion are expected to play a major role. Some substantial differences in the onset of

various types of regular waves were also noted at higher Taylor numbers. *Jonas* [1981] investigated the influence of Prandtl number on the incidence of various forms of vacillation using fluids with Pr ranging from 11 to 74. He reported that amplitude vacillation in particular was significantly more widespread at high Prandtl number, though the onset of "structural vacillation" close to the transition zone at high Taylor number was less sensitive to Pr. In most of the published studies so far, however, the range of Pr investigated has either been limited to relatively high values (using liquids based on water, silicon oils, or organic fluids such as diethyl ether) or very low Pr in liquid metals (mercury).

16.3.1. Transition Between Successive Wave Numbers in Air-Filled Cavity Pr = 0.7

The geometric configuration corresponds to the one used by *Fowlis and Hide* [1965] in their experimental studies of liquids, defined by an inner radius $a = 34.8$ mm, outer radius $b = 60.2$ mm, and height $d = 100$ mm. The cavity is filled with air, Pr = 0.7, and a temperature difference $\Delta T = 30$ K is imposed between the two cylinders. For the rotation rate values considered, a resolution of $N \times M \times K = 64 \times 96 \times 80$ was used in the radial, vertical, and azimuthal directions, respectively, with a dimensionless time step $\delta t = 0.1125$. The results are part of a previous work [*Randriamampianina et al.*, 2006].

Before our numerical investigations of the baroclinic instability using air as working fluid [*Randriamampianina et al.*, 2006], there was not yet any available experimental study devoted to this fluid with Pr = $\mathcal{O}(1)$. However, our findings have subsequently motivated the installation of a specific experimental rig at the university of Oxford, UK [*Castrejón-Pita and Read*, 2007]. Then the measurements confirmed a posteriori the computed results, especially the route to obtain the AV regime. Indeed, unlike in previous experimental works involving liquids, where the onset of the m AV regime was associated with a decrease of the rotation rate from the established steady wave regime mS (defined by a dominant azimuthal wave number m), the AV regime was observed when increasing the rotation rate in this study with air, during the transition between two successive steady waves regime, from an azimuthal wave number m to $m + 1$.

Hide [1958] reported that the transition from axisymmetric to regular wave regimes does not significantly depend on the value of the Prandtl number but rather depends on the thermal Rossby number through the empirical criterion $\Theta \leq \Theta_c = 1.58 \pm 0.05$. In the present simulation, the first regular steady wave was obtained for $\Theta = 1.488 < \Theta_c$ at $Ta = 1.8 \times 10^5$ [*Randriamampianina et al.*, 2006]. In Figure 16.1 we display the bifurcation

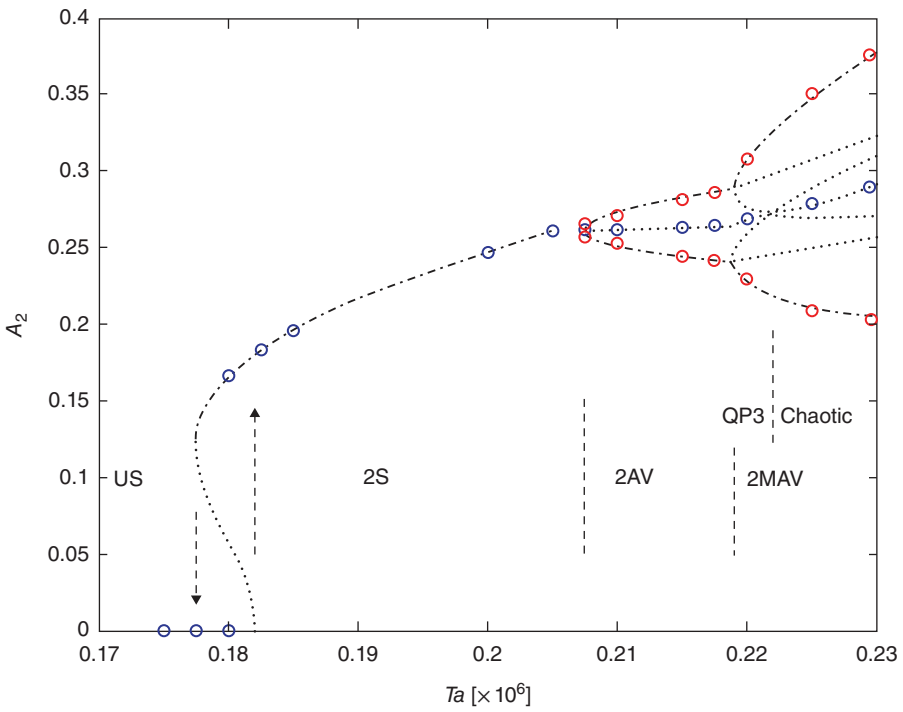

Figure 16.1. Amplitude of the dominant azimuthal wave number mode at midradius and midheight versus the Taylor number showing the bifurcation diagram for the transition from the upper symmetric regime to a steady wave and subsequent vacillations for the $m = 2$ flows in the air-filled cavity.

diagram showing the scenario for the transition from the upper symmetric regime to a steady wave and subsequent amplitude vacillations for the $m = 2$ flows. The, albeit narrow, hysteresis at the transition between the axisymmetric flow and the regular steady wave suggests a subcritical Hopf bifurcation, resulting from a zonal symmetry breaking. By using a weakly nonlinear stability analysis in the same air-filled configuration, *Lewis* [2010] confirmed the subcritical Hopf bifurcation observed during our numerical study. While *Hide and Mason* [1978] reported that such an hysteretic behavior was observed only if the upper boundary was a free surface, *Koschmieder and White* [1981] presented evidence for the possibility of small hysteresis in their experimental study of a water-filled cavity. On the other hand, *Castrejón-Pita and Read* [2007], using air as working fluid in their experiments, mentioned the occurrence of the so-called *weak waves*, characterized by $\Theta > \Theta_c$, prior to the onset of fully developed regular waves, but did not observe any hysteresis cycle. During this study, we did not find any hint of such weak waves.

By progressively increasing the rotation rate, the transition sequence from the upper symmetric US flow through all observed two-wave flows follows clear steps of increasing complexity before bifurcating to three-wave steady flow (the number before the letter denotes the dominant azimuthal wave number): US $\rightarrow$ 2S(P) $\rightarrow$ 2AV(QP2) $\rightarrow$ 2MAV(QP3) $\rightarrow$ 2MAV(NP) $\rightarrow$ 3S(P), as illustrated in Figure 16.1 showing the mean amplitude and the envelope of the vacillation. Here, P stands for periodic, QP for quasi-periodic (QP2 is characterized by two incommensurate frequencies, and QP3 by three frequencies) and NP for aperiodic regime. Steady wave solution 2S is obtained for $1.8 \times 10^5 \leq \mathrm{Ta} \leq 2.05 \times 10^5$. The first 2AV regime, at $\mathrm{Ta} = 2.1 \times 10^5$, likely occurs via a secondary Hopf bifurcation from an oscillatory flow, also known as a Neimark-Sacker bifurcation through a temporal symmetry breaking. It is characterized by a second frequency (QP2) resulting from the periodic oscillations of the amplitude, in addition to the wave drift observed during the regular steady flow. A further increase in rotation rate brings a third frequency coming from the modulation of the amplitude oscillations in the 2MAV regime. This corresponds to a continuation of "the quasi-periodic route to chaos" described by *Newhouse et al.* [1978], but the nature of the initial solution as a quasi-periodic 2MAV with three incommensurate frequencies was unusual. As shown by *Newhouse et al.* [1978], generic three-frequency flows are expected to be chaotic rather than periodic. To our knowledge, no previous example of such a flow has been reported from either numerical or experimental studies of baroclinic waves. The final type of flow dominated by $m = 2$ was a chaotic 2MAV regime that can be induced by a crisis as discussed in a similar baroclinic cavity by *Read et al.* [1998], in analogy with a noise-induced crisis in a multistable system (see also *von Larcher and Egbers* [2005]). Crisis is characterized by a sudden change in the flow dynamics and temporal behavior [see *Grebogi et al.*, 1983]. A further increase in rotation rate up to $\mathrm{Ta} = 2.3 \times 10^5$ from this chaotic solution leads abruptly to the steady 3S regime, also due to a crisis. The temporal behaviors of all the AV and MAV solutions have been confirmed by the calculations of the corresponding largest Lyapunov exponent, reported in Figure 16.2. The quasi-periodic solutions have a largest Lyapunov exponent which cannot be distinguished from zero within the margin of error, while chaotic solutions are characterized by a positive Lyapunov exponent: $2.2 \times 10^5 < \mathrm{Ta} < 2.3 \times 10^5$ [*Randriamampianina et al.*, 2006].

16.3.2. Liquid-Filled Cavity: Pr = 16

The details of the system, the fluid properties, and the governing parameters are summarized in Table 16.1. The configuration corresponds to one experimental rig used at the University of Oxford, UK [*Wordsworth*, 2009]. It consists of an annular domain of inner radius $a = 4.5$ cm, outer radius $b = 15$ cm, and height $d = 26$ cm. The cavity is filled with a liquid described by a Prandtl number $\mathrm{Pr} = 16$ and is submitted to a temperature difference $\Delta T = 2$ K between the inner, cold, and outer, hot, cylinders closed by horizontal insulating rigid endplates. Four values of the rotation rate have been considered, covering different flow regimes of baroclinic waves. For $\Omega = 0.25$, 0.35, and 0.5125 rad/s, a mesh of $N \times M \times K = 128 \times 150 \times 256$ was used in the radial, axial, and azimuthal directions, respectively, with a dimensionless time step $\delta t = 0.0125$. For the rotation rate value $\Omega = 1.25$ rad/s, a refined resolution in the radial and azimuthal directions was necessary, $N \times M \times K = 150 \times 150 \times 320$, with a dimensionless time step $\delta t = 0.00625$.

The values of the control parameters used in the numerical simulation of the flow at these four rotation rates are represented in Figure 16.3 together with the experimental cases considered by *Wordsworth* [2009] in a (Ta, Θ) regime diagram. The slight difference between the measurements and the computations along the traverse corresponding to the temperature difference $\Delta T = 2$ K in Figure 16.3 results from the change operated on the outer radius of the experimental setup when drawing the diagram ($b_{\mathrm{exp}} = 14.3$ cm instead of the value $b = 15$ cm used in the simulations; see Table 16.1). However, no significant differences were observed on the nature of the flow regime between measurements and computed solutions at identical control parameter values. Thus, in agreement with experimental investigations, the first value at $\Omega = 0.25$ rad/s, corresponding to $(\Theta, \mathrm{Ta}) = (2.3475, 2.95 \times 10^6)$, yields a weak wave flow, while for the two others, at Ω values of 0.35

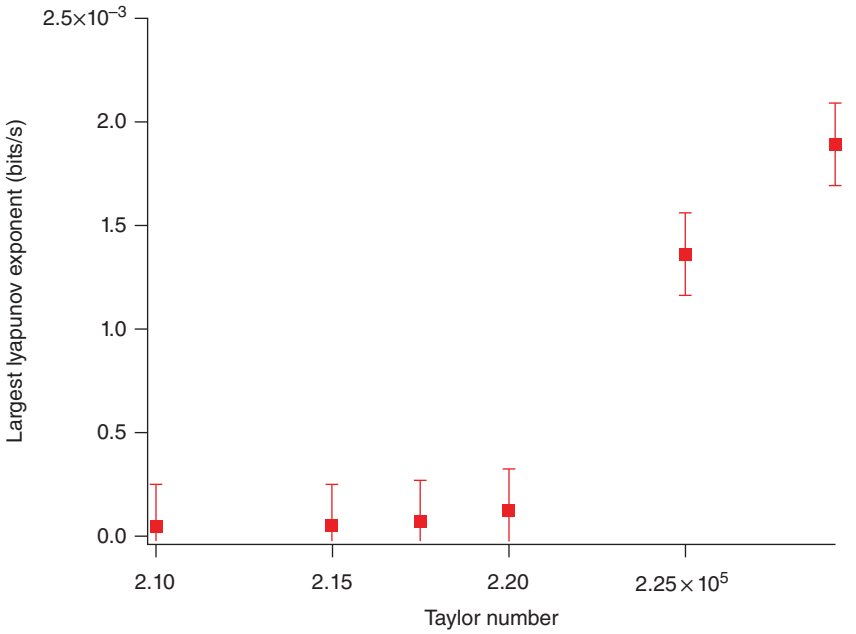

Figure 16.2. Largest Lyapunov exponent for the 2AV and 2MAV flows versus the Taylor number in the air-filled cavity.

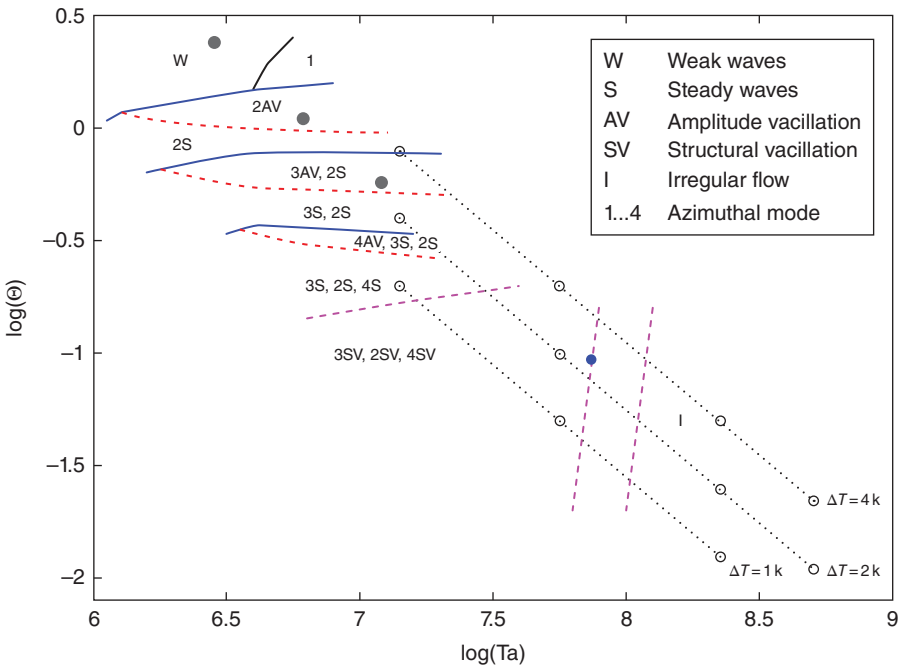

Figure 16.3. Regime diagram in the (Ta, Θ) plane for the liquid-filled cavity with Pr = 16 established from experimental investigations [*Wordsworth*, 2009]; the control parameter values from the measurements are represented by circles and from the computations by dots along the line for ΔT = 2 K. The traverses in dotted lines correspond to values obtained when varying the rotation rate at fixed temperature difference ΔT (here 1 K, 2 K and 4 K). The continuous lines in blue indicate the transition between two flow regimes defined by different azimuthal dominant wave numbers, while the dashed lines in red delimit the transition between two types of temporal dependency.

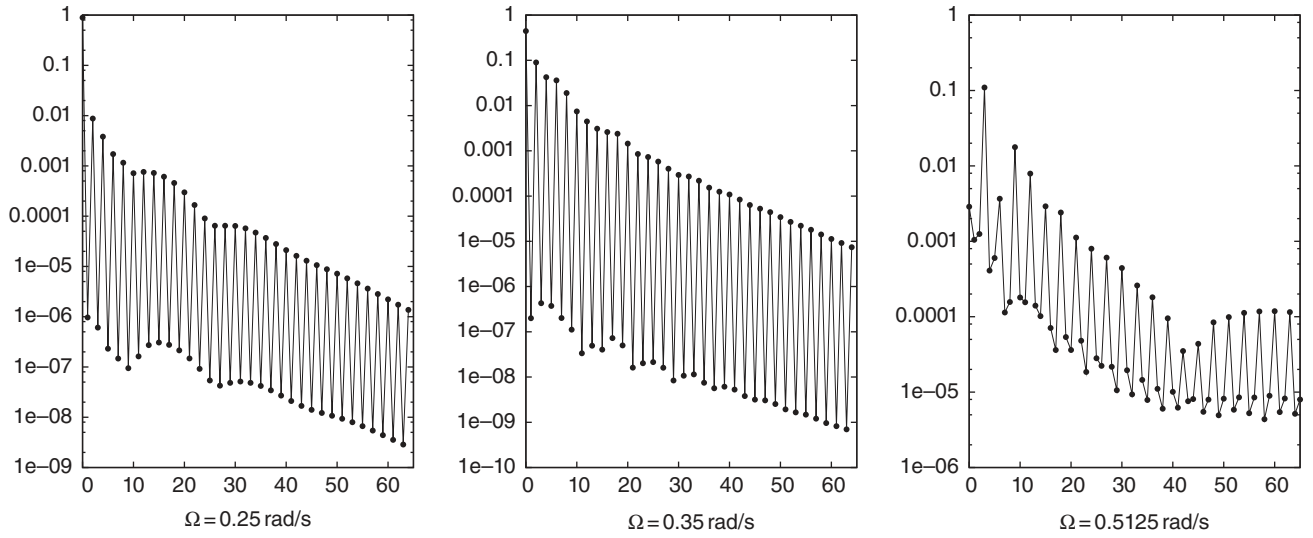

Figure 16.4. Spatial spectra of the time-averaged amplitudes of the azimuthal wave mode m of the temperature at midradius and midheight in the liquid-filled cavity, Pr = 16.

and 0.5125 rad/s, located at $(\Theta, \mathrm{Ta}) = (1.1977, 5.78 \times 10^6)$ and $(0.5586, 1.24 \times 10^7)$ in the regime diagram, the flow evolves to a regular wave flow regime, characterized temporally by an amplitude vacillation but with different dominant azimuthal wave numbers: 2AV and 3AV, respectively. Even though experimental data were not available at these three specific values o f the rotation rate, the regime diagram established from experiments pointed out the existence of these regimes at the corresponding control parameter values, as is cleary shown in Figure 16.3. The rotation rate $\Omega = 1.25$ rad/s with $(\Theta, \mathrm{Ta}) = (0.0939, 7.37 \times 10^7)$ leads to a structural vacillation 3SV regime close to the transition zone as revealed by measurements. In the remainder of this section, comparisons of computed solutions with available experimental data [*Wordsworth*, 2009] are carried out for this rotation rate. Finally, preliminary results from a first attempt to obtain a turbulent flow using direct numerical simulation are discussed and compared with measurements [*Wordsworth*, 2009].

16.3.2.1. Weak Waves. At the lowest value of rotation rates considered, $\Omega = 0.25$ rad/s $(\mathrm{Ta} = 2.95 \times 10^6)$, the simulation predicts a "weak wave" flow regime with a dominant azimuthal wave number $m = 2$, in agreement with experimental findings, as can be seen in Figure 16.3. Similar to the observations of *Castrejón-Pita and Read* [2007] during their experimental investigations in an air-filled cavity, the corresponding thermal Rossby number $\Theta = 2.3475$ is larger than the empirical critical value $\Theta_c = 1.58 \pm 0.05$ determined by *Hide* [1958] for the occurrence of a regular wave regime. This particular flow, developing prior to the onset of regular steady wave, is characterized by a small amplitude of the azimuthal variations of the temperature, $A_m/\Delta T < 0.01$ [*Hide and Mason*, 1978], where m refers to the dominant azimuthal wave number. Figure 16.4 shows the time-averaged spatial spectra of the amplitude of the azimuthal wave mode from Fourier analysis of the temperature at midradius and midheight $(r_{\mathrm{mid}}, z_{\mathrm{mid}})$. The fractional amplitude of the temperature $A_2/\Delta T \sim 0.005$ at $\Omega = 0.25$ rad/s is about 10 times smaller than that of the regular waves obtained at higher rotation rates, $\Omega = 0.35$ $(A_2/\Delta T)$ and 0.5125 rad/s $(A_3/\Delta T)$, for which $\Theta < \Theta_c$. Similar behaviors have been mentioned by *Castrejón-Pita and Read* [2007] from their experimental investigations of weak waves in an air-filled cavity. Moreover, it was found that the computed flow structure toward the upper half of the cavity remains broadly axisymmetric while the baroclinic waves are trapped toward the bottom of the cavity (Figure 16.5). This is consistent with the observations of *Hide and Mason* [1978] using liquids, but in contrast with the flow pattern reported by *Castrejón-Pita and Read* [2007] using air as working fluid with the weak waves visible at all heights of the cavity. This difference can be explained by the thermal stratification levels resulting from the different fluid properties, e.g., the Prandtl number. In the case of air, the Prandtl number is one order of magnitude lower than in liquids, leading to a more uniform density gradient along the vertical direction than in liquids, where a higher density gradient prevails in the lower part of the cavity. As a consequence, the baroclinic instability first develops near the bottom region in cavities filled with liquids.

Another feature of the weak waves comes from their angular drift velocity relative to the cavity. *Hide and Mason* [1978] found that weak waves drifted faster that the

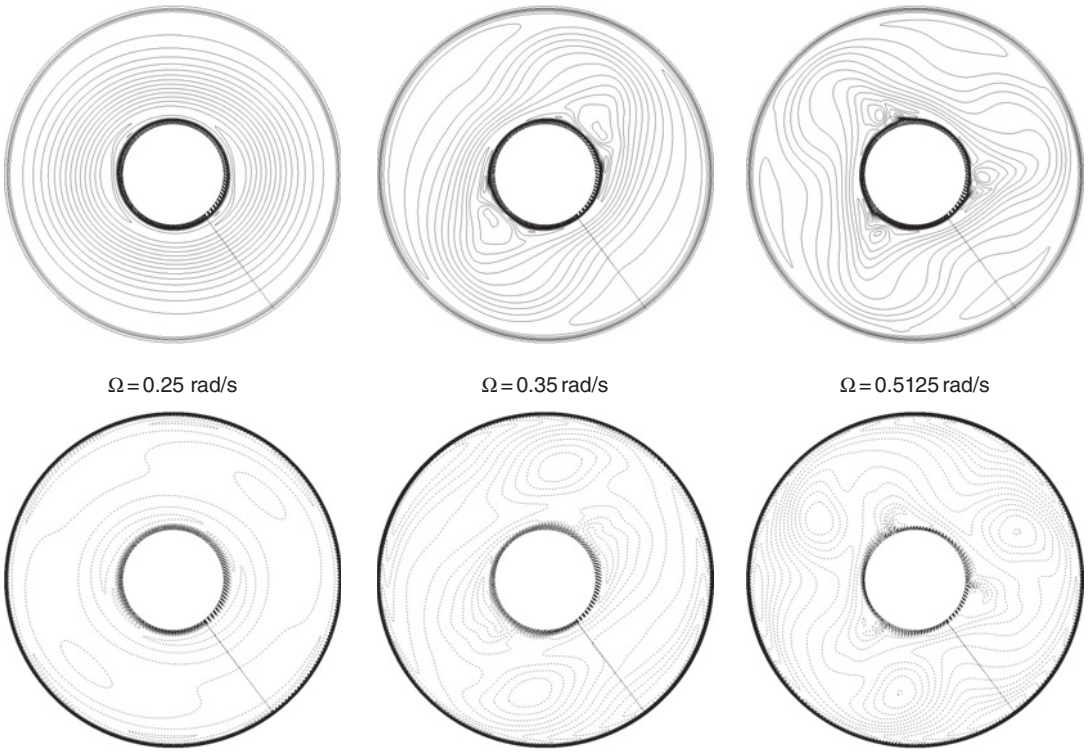

Figure 16.5. Instantaneous isotherms for the three rotation rate values at different heights of the liquid-filled cavity: top at midheight $z/d = 0.5$, bottom at $z/d = 0.19$.

strong waves, and *Castrejón-Pita and Read* [2007] reported a ratio up to 10 in their air-filled experiment. In our case, for the dimensionless drift frequency, we have obtained a ratio of 2 between the weak wave at $\Omega = 0.25$ rad/s and the next strong wave at $\Omega = 0.35$ rad/s, and a ratio of 1.22 between the two regular waves. These behaviors are consistent with the measurements of *Hide and Mason* [1978] in a liquid-filled cavity, keeping in mind that the computed solutions at $\Omega = 0.25$ rad/s and $\Omega = 0.35$ rad/s are characterized by the same dominant wave number $m = 2$, while at $\Omega = 0.5125$ rad/s, the dominant azimuthal wave number is $m = 3$. Both experimental investigations, using liquids [*Hide and Mason*, 1978] or air [*Castrejón-Pita and Read*, 2007], mentioned the marked transition between weak and strong waves. It is concluded that the presence of weak waves prevents the occurrence of a hysteresis cycle during the transition from the upper symmetric regime to regular waves, as these two phenomena were not observed simultaneously.

To our knowledge, the present numerical study represents the first simulation cleary showing such a weak wave flow occurring prior to the regular wave regime within a baroclinic cavity, in agreement with experimental findings.

16.3.2.2. Amplitude Vacillation Flow Regime. At Ω values of 0.35 and 0.5125 rad/s, corresponding to $(\Theta, \mathrm{Ta}) = (1.1977, 5.78 \times 10^6)$ and $(0.5586, 1.24 \times 10^7)$, respectively, in Figure 16.3, the simulation predicts two regular wave regimes characterized spatially by dominant azimuthal wave numbers $m = 2$ and $m = 3$, respectively, as revealed by instantaneous isotherms in Figure 16.5 and temporally by an amplitude vacillation. These solutions have been directly obtained by progressively increasing the rotation rate; e.g., the solution at the higher rotation rate $\Omega = 0.5125$ rad/s was computed using as initial conditions the one at lower rotation rate $\Omega = 0.35$ rad/s. The simulations were not able to capture any steady regular wave flow, although experiments reported 2S and 3S regimes in Figure 16.3, keeping in mind that 2AV (3AV) regimes resulted experimentally from steady waves 2S (3S) by decreasing the rotation rate (see Chapter 3). Moreover, as soon as the large-scale regular baroclinic structures arise, we have observed the spontaneous development of small-scale fluctuations particularly along the cold inner cylinder, even though experimental studies did not mention such a behavior. However, it can be explained by possible technical limitations to detect the very low level of these fluctuations at these rotation rates [*Read*, 1992]. Thus, in some particular regions, the computed flow exhibits locally a spatiotemporal chaotic behavior. As introduced previously by *Randriamampianina et al.* [2006] to describe the temporal characteristics, we use the

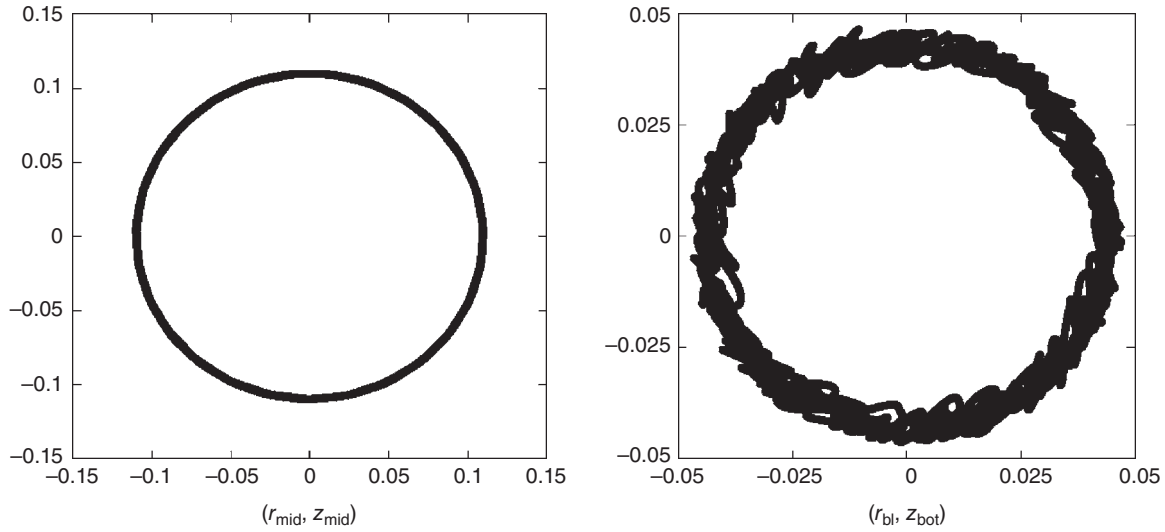

Figure 16.6. Phase space diagrams of the temperature field at two fixed *(r, z)* locations for Ω = 0.5125 rad/s in the liquid-filled cavity, Pr = 16, showing the time series of the sine component versus that of the cosine component of the azimuthal dominant mode $m = 3$.

representation in the phase space based on time series of cosine and sine components of the dominant azimuthal wave number from a Fourier analysis of the temperature at two specific fixed (r, z) locations. We display these behaviors in Figure 16.6 at Ω = 0.5125 rad/s, for which the intensity of the small-scale features was found highest between the computed AV solutions. In agreement with the experimental findings of *Wordsworth* [2009], the first plot at midradius and midheight (r_{mid}, z_{mid}) shows a "classical" 3AV profile defined by two frequencies: the wave drift represented by the large circle and the periodic oscillations of the wave amplitude, both related to the baroclinic instability [*Randriamampianina et al.*, 2006]. The second map, taken at a radius location r_{bl} inside the boundary layer along the inner cold cylinder and at a height near the bottom wall, z_{bot}, clearly exhibits a chaotic behavior corresponding to a 3MAV regime.

Since such different AV and MAV regimes were not observed simultaneously under fixed values of control parameters within the air-filled cavity [*Randriamampianina et al.*, 2006] but successively when increasing the values of rotation rate as shown in Figure 16.1, this localized 3MAV is directly ascribed to the presence of small-scale features. From their recent direct numerical simulation in a liquid-filled baroclinic cavity with Pr = 24.47, *Jacoby et al.* [2011] identified these small structures, occurring spontaneously and simultaneously with the large-scale baroclinic waves, as inertia-gravity waves (IGWs). The characteristics of the IGWs observed in the present configuration are discussed by *Randriamampianina* [2013]. The values of the sine and cosine components reported in Figure 16.6 are related to IGW activity, more specifically to the balance between the two phenomena involved, with highest values associated with baroclinic instability. It reflects the variability of IGWs and the interaction between these two waves characterized by very different scales in time and in space. In particular, it puts forward the ability of the IGWs to induce locally a chaotic regime of the large-scale flow motion. Such a behaviour was not mentioned either by experiments [*Wordsworth*, 2009] or by previous simulations using liquids [*Hignett et al.*, 1985; *Jacoby et al.*, 2011]. From their numerical simulation based on finite difference approximation, *Hignett et al.* [1985] obtained also the AV regime, using a liquid defined by Pr = 13.07, but did not report the presence of these small-scale features. On the other hand, we did not observe the appearance of these fluctuations simultaneously with baroclinic waves when considering air in the present geometry, but rather we found the same flow structures reported by *Randriamampianina et al.* [2006] for air using different geometric dimensions. It clearly reveals the strong dependence on the Prandtl number of the baroclinic instability characteristics through the thermal stratification of the flow. Again we refer the reader to Chapter 3 in this book about the detailed analysis of the amplitude vacillation flow regime, particularly about the different mechanisms responsible for their occurrence.

16.3.2.3. Structural Vacillation Flow Regime. In spite of a well-defined dominant azimuthal wave number, this flow is characterized by the presence of small-scale fluctuations which progressively destroy the regularity of

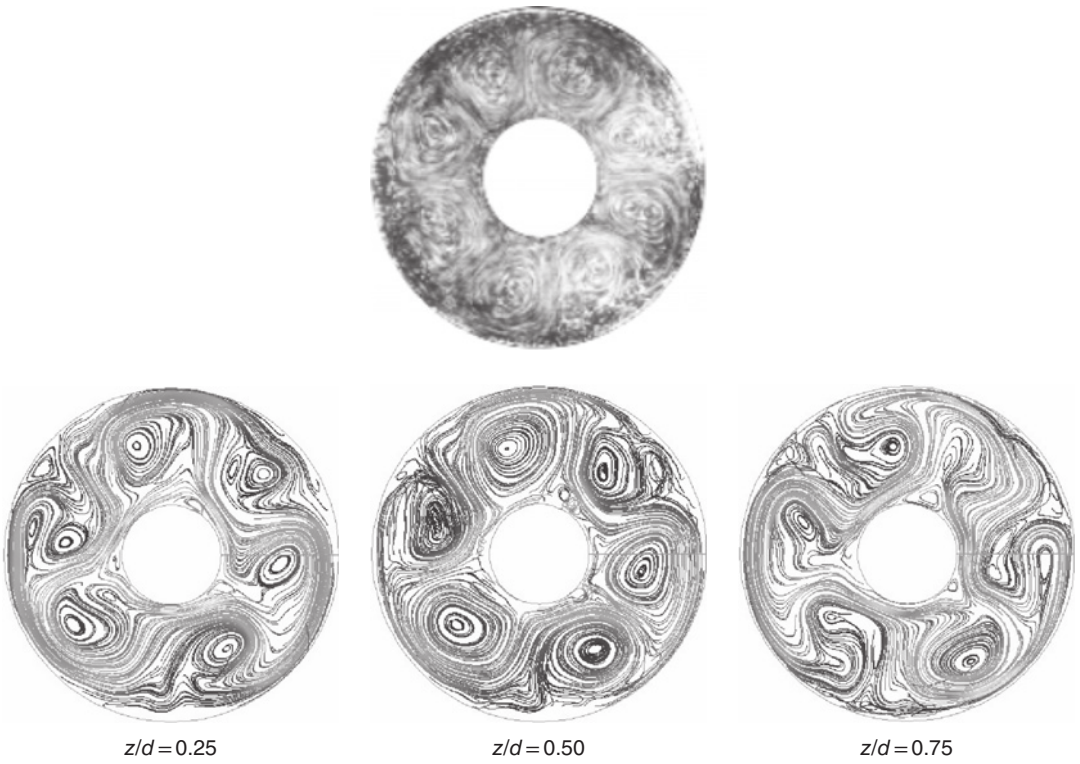

Figure 16.7. Comparison of flow structures between experimental measurements at midheight z/d = 0.50 (top) and computed solutions at different heights (bottom) for the structural vacillation regime in the liquid-filled cavity, Pr = 16.

the large-scale baroclinic waves and therefore eventually lead to disordered flow [*Früh and Read*, 1997; *Read et al.*, 2008]. We have carried out comparisons of flow structures between our computed results and laboratory measurements obtained by *Wordsworth* [2009] (see also *Wordsworth et al.* [2008]). The rotation rate used in the experimental study was $\Omega = 1.3$ rad/s while in the simulation $\Omega = 1.25$ rad/s was used, corresponding to $(\Theta, \mathrm{Ta}) = (0.0939, 7.37 \times 10^7)$, which is located close to the transition zone in the regime diagram (Figure 16.3), with a temperature difference ΔT = 2 K. In both cases, a SV regime was obtained. The experiment reported 4SV, as revealed by instantaneous streaklines in Figure 16.7, but also 3SV as seen in Figure 16.8 from the azimuthal velocity and axial vorticity in a horizontal plane. This situation reflects the intransitivity phenomenon, inherent to rotating flows in cavities, with the coexistence of different stable flow structures, e.g., different dominant azimuthal wave numbers, under the same imposed external conditions (see also Figure 16.3). The simulation predicts a 3SV regime. The flow exhibits a chaotic behavior induced by the random presence of small-scale fluctuations over an almost regular arrangement of waves at midheight ($z/d = 0.5$), as can be seen in Figure 16.7. Such a flow structure was already observed in a rotating cavity under symmetrical boundary conditions to ensure mass conservation due to the antisymmetry of the flow with respect to the midheight [*Randriamampianina et al.*, 2001]. In particular, it is clearly visible in Figure 16.7 from the two instantaneous computed streaklines at different heights $z/d = 0.25$ and $z/d = 0.75$ located symmetrically with respect to the midheight, the onset and the growth of additional structures randomly induce the breakdown of the regularity of the large-scale baroclinic waves. This phenomenon, associated with the loss of symmetry of waves, known to be characteristic of the structural vacillation regime, ultimately leads to the fully disordered flow. The IGWs mentioned above at lower rotation rate values, $\Omega = 0.35$ rad/s and $\Omega = 0.5125$ rad/s, are found to be the small-scale fluctuations responsible for the chaotic behavior of this SV flow, in contrast with the air-filled cavity where the mechanism of transition resulted from radial buoyancy in a Rayleigh-Bénard-like rotating flow [*Read et al.*, 2008]. In the latter case the centrifugal acceleration was greater than the gravity everywhere inside the cavity, giving a local Froude number $\mathrm{Fr}_r \equiv \Omega^2 r^*/g > 1$, $r^* \in [a, b]$, while in the present computations, $\mathrm{Fr} = 1.67 \times 10^{-2}$ (see Table 16.1).

We have compared the instantaneous contours of the azimuthal velocity and of the axial component of the vorticity between the available experimental measurements [*Wordsworth*, 2009] and the computed solutions at midheight in Figure 16.8. We note the overall good agreement

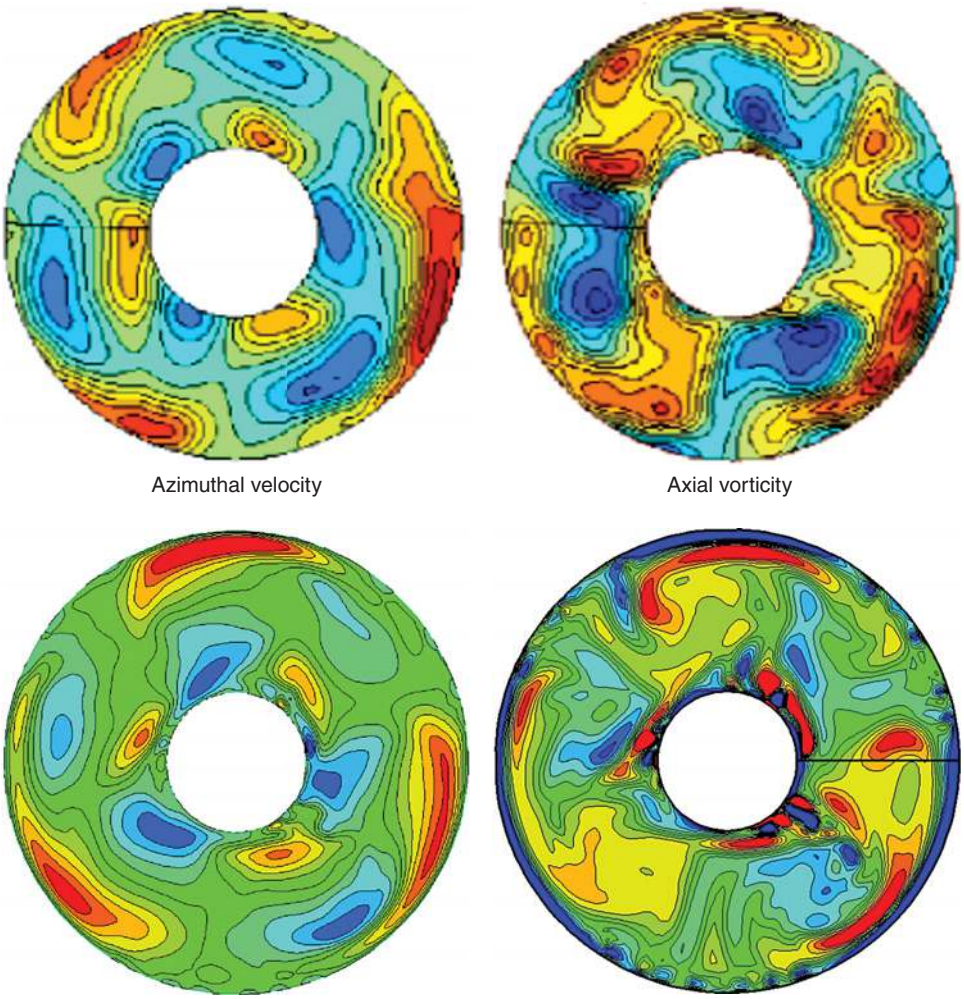

Figure 16.8. Comparison of flow characteristics at midheight between experimental measurements (top) and computed solutions (bottom) for the structural vacillation regime in the liquid-filled cavity, Pr = 16. For color detail, please see color plate section.

of the flow patterns obtained with the two approaches, in particular the similarity of large-scale structures, characterized by the same dominant azimuthal wave number $m = 3$. The slight discrepancy may result from the different isovalues chosen on contours by each approach. We note the presence of small-scale fluctuations initially developing along the inner cold wall, identified as IGWs and postulated to be the main mechanism responsible for the spatiotemporal chaotic behavior during the transition to turbulent flow regimes. Indeed, these small-scale features are expected to grow randomly in the whole cavity for the irregular waves. We refer to *Wordsworth et al.* [2008] for a detailed analysis of the experimental investigations.

16.3.2.4. Irregular Wave Regime. Direct numerical simulation was carried out to provide a first attempt to obtain the irregular wave regime in a baroclinic cavity and to compare the results with experimental data provided by *Wordsworth* [2009] (see also *Wordsworth et al.* [2008]). The imposed external conditions represent a temperature difference between the two cylinders of $\Delta T = 2$ K with a rotation rate $\Omega = 3$ rad/s for the simulation, corresponding to $\Theta = 0.016$ and $\mathrm{Ta} = 4.25 \times 10^8$, while for the experiment $\Omega = 3.9$ rad/s. The mesh used was $N \times M \times K = 256 \times 128 \times 512$ in the radial, axial, and azimuthal directions, respectively, with a dimensionless time step $\delta t = 0.000125$. The preliminary computed solution is compared with experimental measurements in Figure 16.9, showing the complex flow structure, where any dominant azimuthal wave number can be extracted as in the SV regime discussed above (see also the Figure 3 presented by *Wordsworth et al.* [2008]). The solution is obviously still far from its asymptotic state. However, this first result demonstrates the ability of the present numerical tool to compute the complex irregular waves in baroclinic cavities. The computed structures mimic very well the streak photographs illustrating irregular waves reported by *Hide and Mason* [1975] from their experimental studies in a

Figure 16.9. Comparison between experimental visualization and computed solution for the irregular wave regime in the liquid-filled cavity, Pr = 16.

water-filled cavity. *Wordsworth et al.* [2008] reported a detailed analysis of the experimental investigations. The prohibitive CPU time cost resulting from an adequate mesh resolution required to resolve all the scales of the flow did not allow statistical convergence in a reasonable time. It also points out the actual limitations of computing power. An extension of the present numerical tool to parallel machines is in progress by implementing a domain decomposition technique, which should allow sufficient resolution to capture all the turbulence scales.

16.3.3. Open Free-Surface Water-Filled cavity: Pr = 7

Preliminary results are reported for an open upper free-surface cavity using water as working fluid, Pr = 7, and compared with available measurements from *K. Alexandrov, Y. Wang, U. Harlander, and C. Egbers (DFG-MetStroem reference experiment, BTU, Cottbus, Germany)*. The geometric configuration used in the simulation is the one considered above in the liquid-filled cavity, with an inner radius $a = 4.5$ cm, outer radius $b = 15$ cm, and height $d = 26$ cm, while $a = 4.5$ cm, $b = 12$ cm, and $d = 13.5$ cm in the experimental setup [*Harlander et al.*, 2011]. Comparison concerns the tem-perature distribution at the upper free surface for a regular wave flow. It is recognized that the occurrence of baroclinic instability does not depend on the presence or absence of a top lid [*Hide and Mason*, 1978], even though significant differences can be observed. The open free surface, by inducing a shear flow, triggered by the use of Neumann conditions at this boundary in the numerical simulation, yields a motion at this top height with the associated temperature behavior. On the other hand, in the presence of a rigid lid, a part of the upper region remains at the same temperature as the outer hot wall, as was observed in the liquid-filled cavity with Pr = 16 [*Randriamampianina*, 2013]. Moreover, at low rotation rate for the later fluid in the weak wave regime, baroclinic instability was found to develop first near the bottom wall due to higher density gradient level toward this region (see Figure 16.5).

We display in Figure 16.10 the instantaneous temperature field at the open upper free surface obtained from simulation and infrared thermography. As different external conditions were used for the simulation ($\Delta T = 2$ K, $\Omega = 0.8$ rad/s) and for the experiment with $\Delta T = 8$ K, $\Omega = 0.47$ rad/s, the figure is presented to show qualitative behavior for a three-wave flow between the two approaches. It appears that the computed result did not yet reach the asymptotic state, as revealed by the asymmetry of the waves, in comparison with the measurements. *Harlander et al.* [2012] mentioned from their experimental investigations that a complete cycle can take about 27 revolutions. However, an overall agreement can be observed, in particular a pronounced incursion of "hot plumes" recirculating from the external hot cylinder toward the center of the cavity along the anticyclonic vortices, associated with a strong acceleration as seen from the superimposed velocity field. Such wave asymmetry can also be attributed to wave interaction during the establishment of baroclinic instability, as reported by *Harlander et al.* [2012].

16.4. CONCLUSIONS

Direct numerical simulations based on high-resolution pseudospectral methods were carried out for the investigation of the complex flow regimes occurring in a differentially heated rotating cylindrical annulus, the baroclinic cavity. The computed solutions have been compared with available laboratory measurements in configurations having an insulating top lid or an open free

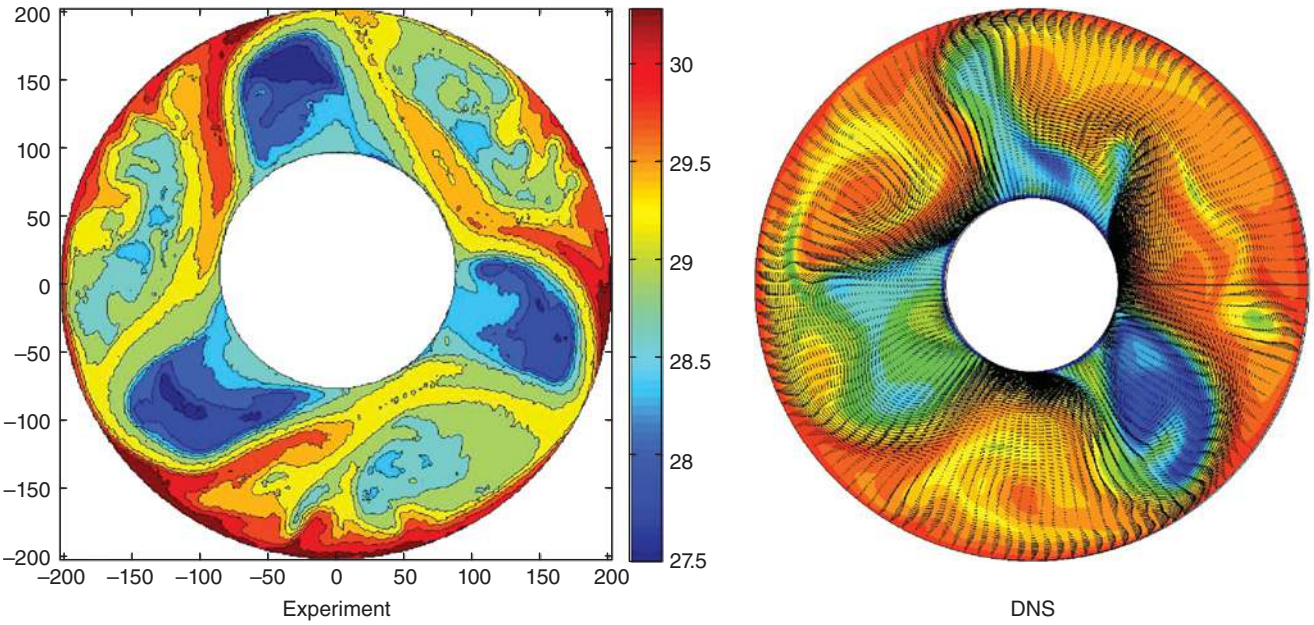

Figure 16.10. Instantaneous temperature field at the open upper free surface for the water-filled cavity. For color detail, please see color plate section.

surface. The approach was applied to describe the various spatiotemporal characteristics of baroclinic waves using three different fluids. It has allowed for a detailed analysis of the features observed during laboratory measurements. The results demonstrate the ability of the present numerical tool to reproduce the complex spatiotemporal behaviors and to capture the small-scale fluctuations responsible for the break of the regular waves to chaotic motion in baroclinic cavities. The simulations report the first realistic solutions of weak waves and structural vacillation regimes for liquids and amplitude vacillation for air, in agreement with experimental observations. Moreover, the computations point out the important role played by the Prandtl number on the baroclinic instability characteristics due to the differences in the thermal stratification levels. In particular, at high values of the Prandtl number, the spontaneous generation of IGWs was found simultaneously with the large-scale baroclinic waves. These small-scale features, initially developing along the inner cold cylinder, are postulated to be the mechanism responsible for the transition to irregular flows.

The extension of the approach to parallel computing, by implementing a domain decomposition technique, is in progress and is expected to allow for a direct numerical simulation of the fully developed turbulent flow regime in the baroclinic cavity.

Acknowledgments. The authors would like to acknowledge fruitful discussions with T. Jacoby and P. L. Read (AOPP, Oxford, UK), W.-G. Früh (SEPS, Heriot-Watt University, Edinburgh, UK), and R. Plougonven (LMD, Paris, France). The authors are indebted to R. Wordsworth (AOPP, Oxford, UK), U. Harlander, and C. Egbers (BTU, Cottbus, Germany) for their help in providing experimental measurements. The authors are grateful to the Spanish government for financial support, research project number FIS2011-24642. This work was granted access to the HPC resources NEC-SX8 of CCRT (CEA, France) and NEC-SX5 of IDRIS (CNRS, France) under the allocation 21444 made by GENCI (Grand Equipement National de Calcul Intensif). The authors are grateful to the anonymous referees for their constructive criticisms and suggestions.

REFERENCES

Alexandrov, K., Y. Wang, U. Harlander, and C. Egbers, DFG-MetStroem reference experiment, BTU, Cottbus, Germany.

Canuto, C., M. Hussaini, A. Quarteroni, and T. Zang (1987), *Spectral Methods in fluid Dynamics*, Springer-Verlag, Berlin.

Castrejón-Pita, A. A., and P. L. Read (2007), Baroclinic waves in an air-filled thermally driven rotating annulus, *Phys. Rev. E*, *75*, 026,301, doi:10.1103/PhysRevE.75.026301.

Chaouche, A. M., A. Randriamampianina, and P. Bontoux (1990), A collocation method based on an influence matrix technique for axisymmetric flows in an annulus, *Comp. Meth. Appl. Mech. Eng.*, *80*, 237–244.

Fein, J. S., and R. L. Pfeffer (1976), An experimental study of the effects of Prandtl number on thermal convection in a rotating, differentially heated cylindrical annulus of fluid, *J. Fluid Mech.*, *75*, 81–112.

Fowlis, W. W., and R. Hide (1965), Thermal convection in a rotating annulus of liquid: Effect of viscosity on the transition

between axisymmetric and non-axisymmetric flow regimes, *J. Atmos. Sci.*, *22*, 541–558.

Früh, W- G., and P. L. Read (1997), Wave interactions and the transition to chaos of baroclinic waves in a thermally driven rotating annulus, *Phil. Trans. R. Soc. Lond. A, 355*, 101–153.

Gottlieb, D., and S. Orszag (1977), *Numerical Analysis of Spectral Methods: Theory and Applications*, CBMS-NSF Regional Conference Series in Applied Mathematics, SIAM, Philadelphia, Pennsylvania, USA.

Grebogi, C., E. Ott, and J. A. Yorke (1983), Crises, sudden changes in chaotic attractors, and transient chaos, *Phys. D*, *7*, 181–200.

Haldenwang, P., G. Labrosse, S. Abboudi, and M. Deville (1984), Chebyshev 3-d spectral and 2-d pseudospectral solvers for the Helmholtz equation, *J. Comput. Phys.*, *55*, 115–128.

Harlander, U., T. von Larcher, Y. Wang, and C. Egbers (2011), PIV- and LDV-measurements of baroclinic wave interactions in a thermally driven rotating annulus, *Exp. Fluids*, *51*, 37–49.

Harlander, U., J. Wenzel, K. Alexandrov, Y. Wang, and C. Egbers (2012), Simultaneous PIV and thermography measurements of partially blocked flow in a differentially heated rotating annulus, *Exp. Fluids*, *52*, 1077–1087.

Hide, R. (1958), An experimental study of thermal convection in a rotating fluid, *Philos. Trans. R. Soc. Lond.*, *A250*, 441–478.

Hide, R., and P. J. Mason (1975), Sloping convection in a rotating fluid, *Adv. Phys.*, *24*, 47–100.

Hide, R., and P. J. Mason (1978), On the transition between axisymmetric and non-axisymmetric flow in a rotating liquid annulus subject to a horizontal temperature gradient, *Geophys. Astrophys. Fluid Dyn.*, *10*, 121–156.

Hignett, P., A. A. White, R. D. Carter, W. D. N. Jackson, and R. M. Small (1985), A comparison of laboratory measurements and numerical simulations of baroclinic wave flows in a rotating cylindrical annulus, *Q. J. R. Met. Soc.*, *111*, 131–154.

Hugues, S., and A. Randriamampianina (1998), An improved projection scheme applied to pseudospectral methods for the incompressible Navier-Stokes equations, *Int. J. Numer. Meth. Fluids*, *28*, 501–521.

Jacoby, T. N. L., P. L. Read, P. D. Williams, and R. M. B. Young (2011), Generation of inertia-gravity waves in the rotating thermal annulus by a localised boundary layer instability, *Geophys. Astrophys. Fluid Dyn.*, *105*, 161–181.

James, I. N., P. R. Jonas, and L. A. Farnell (1981), A combined laboratory and numerical study of fully developed steady baroclinic waves in a cylindrical annulus, *Q. J. R. Met. Soc.*, *107*, 51–78.

Jonas, P. R. (1981), Some effects of boundary conditions and fluid properties on vacillation in thermally driven rotating flow in an annulus, *Geophys. Astrophys. Fluid Dyn.*, *18*, 1–23.

Koschmieder, E. L., and H. D. White (1981), Convection in a rotating, laterally heated annulus. the wave number transitions, *Geophy. Astrophys. Fluid Dyn.*, *18*, 279–299.

von Larcher, Th., and C. Egbers (2005), Experiments on transitions of baroclinic waves in a differentially heated rotating annulus, *Nonlin. Process. Geophys.*, *12*, 1033–1041.

Lewis, G. (2010), Mixed-mode solutions in an air-filled differentially heated rotating annulus, *Phys. D*, *239*, 1843–1854.

Newhouse, S. E., D. Ruelle, and F. Takens (1978), Occurrence of strange axiom a attractors near quasi-periodic flow on T^m, $m \geq 3$, *Commun. Math. Phys.*, *64*, 35–40.

Orlanski, I., and M. D. Cox (1973), Baroclinic instability in ocean currents, *Geophys. Fluid Dyn.*, *4*, 297–332.

Pierrehumbert, R. T., and K. L. Swanson (1995), Baroclinic instability, *Annu. Rev. Fluid Mech.*, *27*, 419–467.

Pulicani, J. P., E. Crespo Del Arco, A. Randriamampianina, P. Bontoux and R. Peyret (1990), Spectral simulations of oscillatory convection at low Prandtl number, *Int J. Numer. Meth. Fluids*, *10*, 481–517.

Randriamampianina, A. (2013), Inertia gravity waves characteristics within a baroclinic cavity, *Comptes Rendus Mécanique*. *341*, 547–552.

Randriamampianina, A., E. Crespo Del Arco, J. P. Fontaine, and P. Bontoux (1990), Spectral methods for two-dimensional time-dependent $Pr \to 0$ convection, *Notes Numer. Fluid Mech.*, *27*, 244–255.

Randriamampianina, A., E. Leonardi, and P. Bontoux (1997), A numerical study of the effects of Coriolis and centrifugal forces on buoyancy driven flows in a vertical rotating annulus, in *Advances in Computational Heat Transfer*, edited by G. De Vahl Davis and E. Leonardi, Begell House, Cesme, Turkey.

Randriamampianina, A., R. Schiestel, and M. Wilson (2001), Spatio-temporal behaviour in an enclosed corotating disk pair, *J. Fluid Mech.*, *434*, 39–64.

Randriamampianina, A., R. Schiestel, and M. Wilson (2004), The turbulent flow in an enclosed corotating disk pair: Axisymmetric numerical simulation and Reynolds stress modelling, *Int. J. Heat Fluid Flow*, *25*, 897–914.

Randriamampianina, A., W.-G. Früh, P. Maubert, and P. L. Read (2006), DNS of bifurcations in an air-filled rotating baroclinic annulus, *J. Fluid Mech.*, *561*, 359–389.

Raspo, I., S. Hugues, E. Serre, A. Randriamampianina, and P. Bontoux (2002), A spectral projection method for the simulation of complex three-dimensional rotating flows, *Comput. Fluids*, *31*, 745–767.

Read, P. L. (1992), Applications of singular systems analysis to baroclinic chaos, *Phys. D*, *58*, 455–468.

Read, P. L. (2001), Transition to geostrophic turbulence in the laboratory, and as a paradigm in atmospheres and oceans, *Surv. Geophys.*, *22*, 265–317.

Read, P. L., M. Collins, W.-G. Früh, S. R. Lewis, and A. F. Lovegrove (1998), Wave interactions and baroclinic chaos: A paradigm for long timescale variability in planetary atmospheres, *Chaos Solitons Fractals*, *9*, 231–249.

Read, P. L., P. Maubert, A. Randriamampianina, and W.-G. Früh (2008), DNS of transitions towards Structural Vacillation in an air-filled, rotating, baroclinic annulus, *Phys. Fluid*, *20*, 044,107.

Vanel, J. M., R. Peyret, and P. Bontoux (1986), A pseudospectral solution of vorticity-streamfunction equations using the influence matrix technique, in *Numerical Methods in Fluid Dynamics II*, edited by K. W. Morton and M. J. Baines, pp. 463–475, Clarendon Press, Oxford.

Williams, G. P. (1969), Numerical integration of the three-dimensional Navier-Stokes equations for incompressible flow, *J. Fluid Mech.*, *37*, 727–750.

Williams, G. P. (1971), Baroclinic annulus waves, *J. Fluid Mech.*, *49*, 417–449.

Wordsworth, R. D. (2009), Theoretical and experimental investigations of turbulent jet formation in planetary fluid dynamics, Ph.D. thesis, Linacre College, Oxford United Kingdom.

Wordswoth, R. D., P. L., Read, and Y. H. Yamazaki (2008), Turbulence, waves, and jets in a differentially heated rotating annulus experiment, *Phys. Fluid.*, *20*, 126,602.

Zang, T. A. (1990), Spectral methods for simulations of transition and turbulence, *Comp. Meth. Appl. Mech. Eng.*, *80*, 209–221.

Zeytounian, R. Kh. (2003), Joseph Boussinesq and his approximation: A contemporary review, *Comptes Rendus Mécanique*, *331*, 575–586.